RadioGraphics

An Introduction to PET-CT Imaging[1]

Vibhu Kapoor, MD • Barry M. McCook, MD • Frank S. Torok, MD

Cancer is one of the leading causes of morbidity and mortality in developed countries such as the United States. Complex clinical decisions about treatment of oncologic patients are largely guided by imaging findings, among other factors. Most radiologic procedures map the anatomy and morphology of tumors with little or no information about their metabolism. Positron emission tomography (PET) performed with 2-[fluorine-18]fluoro-2-deoxy-D-glucose (FDG) has proved valuable in providing important tumor-related qualitative and quantitative metabolic information that is critical to diagnosis and follow-up. PET–computed tomography (CT) is a unique combination of the cross-sectional anatomic information provided by CT and the metabolic information provided by PET, which are acquired during a single examination and fused. FDG PET–CT offers several advantages over PET alone; the most important is the ability to accurately localize increased FDG activity to specific normal or abnormal anatomic locations, which may be difficult or even impossible with PET alone. Understanding the principles of FDG PET–CT and the optimal scanning techniques and recognizing the potential pitfalls and limitations are important for advantageous use of this imaging modality.

Abbreviation: FDG = 2-[F-18]fluoro-2-deoxy-D-glucose

Index terms: Data fusion • Dual-modality imaging, PET/CT • Fluorine, radioactive, **.12166[2] • Images, fusion • Neoplasms, PET, **.12163, **.12166 • Positron emission tomography (PET), **.12163

RadioGraphics 2004; 24:523–543 • **Published online** 10.1148/rg.242025724

[1]From the Department of Radiology, University of Pittsburgh Medical Center, 200 Lothrop St, Pittsburgh, PA 15213. Received December 12, 2002; revision requested March 24, 2003; final revision received and accepted June 16. **Address correspondence to** V.K. (e-mail: *kapoorv@msx.upmc.edu*).

[2] **. Multiple body systems

Introduction

Positron emission tomography (PET) is being increasingly used for diagnosis, staging, and follow-up of various malignancies. It has been studied in the evaluation of various tumors including but not limited to solitary pulmonary nodules, non–small cell lung carcinoma, lymphoma, melanoma, breast cancer, and colorectal cancer (1–7). Computed tomography (CT) and magnetic resonance (MR) imaging rely on anatomic changes for diagnosis, staging, and follow-up of cancer. However, PET has the ability to demonstrate abnormal metabolic activity (at the molecular level) in organs that as yet do not show an abnormal appearance based on morphologic criteria. It aids in differentiation of malignant from benign lesions and in staging of malignancies. PET is also useful in the follow-up of patients following chemotherapy or surgical resection of tumor, most of whom have a complicating appearance at CT or MR imaging due to postoperative changes or scar tissue.

In certain situations, it may be impossible to accurately localize an area of increased activity on PET images alone due to the absence of identifiable anatomic structures, particularly in the abdomen. Investigators recognized this limitation in oncology imaging, and therefore attempts at developing algorithms to coregister functional and anatomic information have had varying success in the past decade (8–10). Beyer et al (11) described the prototype PET-CT scanner used in clinical imaging, in which precisely coregistered functional and anatomic images could be obtained by performing a PET study and a CT study on the same scanner without moving the patient. Although the limit of resolution of PET alone as compared with that of PET-CT remains the same, the overall combination aids in the accurate localization of regions of increased activity on PET images with greater confidence.

Managed healthcare professionals have recognized the role of PET in the care of oncology patients. At the time of writing this article, reimbursement for PET is approved for characterization of a solitary pulmonary nodule, melanoma, lymphoma, and esophageal, colorectal, head and neck, breast, and non–small cell lung carcinoma. The focus of our discussion will be the principles of 2-[fluorine-18]fluoro-2-deoxy-D-glucose (FDG) PET–CT fusion imaging, with emphasis on the general principles of FDG production, FDG PET imaging, PET-CT fusion, the scanning technique, and clinical applications in oncology.

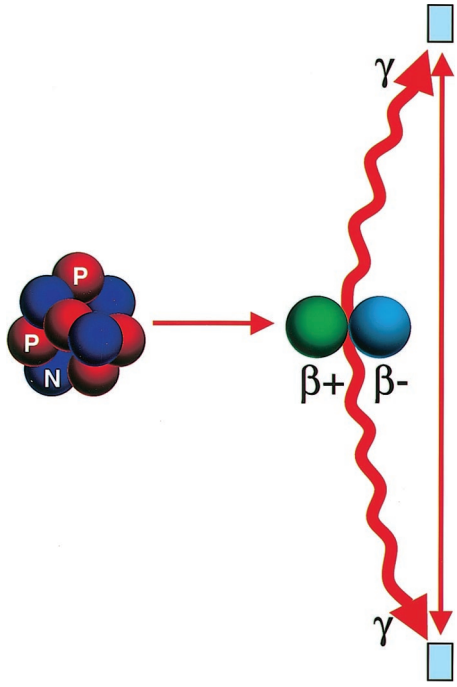

Figure 1. Annihilation reaction. Positrons (β+) released from the nucleus of FDG annihilate with electrons (β−), releasing two coincidence 511-keV photons (γ), which are detected by scintillation crystals (blue rectangles). *N* = neutron, *P* = proton.

General Principles of FDG Production

PET is based on the detection of annihilation photons (γ) released when radionuclides, such as F-18, carbon-11, and oxygen-15, emit positrons (β^+) that undergo annihilation with electrons (Fig 1). The photons thus released have energies of 511 keV (0.511 MeV) and are detected by coincidence imaging as they strike scintillation crystals made of bismuth germinate (BGO), lutetium oxyorthosilicate (LSO), or gadolinium silicate (GSO). The value 511 keV represents the energy equivalent of the mass of an electron according to the law of conservation of energy. Bombarding target material with protons that have been accelerated in a cyclotron produces positron-emitting radionuclides, which are then used to synthesize radiopharmaceuticals that are part of biochemical pathways in the human body, such as FDG in glucose metabolism and C-11–labeled methionine and choline in protein metabolism and membrane biosynthesis, respectively.

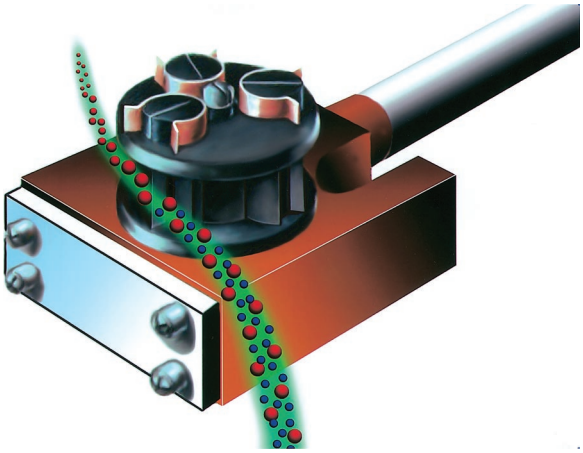

Figure 2. Production of F-18. After acceleration in a cyclotron, negatively charged hydrogen ions (red and blue spheres) pass through a carbon foil in a carousel, which removes the electrons (blue spheres) from the hydrogen ion, leaving behind high-energy protons (red spheres). The protons are directed toward a target chamber that contains stable O-18–enriched water, thus producing hydrogen (F-18) fluoride. (Adapted and reprinted, with permission, from reference 21.)

Production of F-18

F-18 is produced in a cyclotron by bombarding O-18–enriched water with high-energy protons. Negatively charged hydrogen ions are accelerated in a cyclotron till they gain approximately 8 MeV of energy, then the orbital electrons from the ion are removed (Fig 2). The resultant high-energy positive hydrogen ions (H^+) or proton beam is directed toward a target chamber that contains the stable O-18–enriched water molecules. The protons undergo a nuclear reaction with the O-18–enriched water to form hydrogen (F-18) fluoride:

$$H_2(\text{O-18}) + \text{H-1} + \text{energy} \rightarrow H_2(\text{F-18}). \quad (1)$$

O-18 and F-18 are isobars, that is, they have the same mass number (A = nucleons) but different atomic numbers (Z is 8 for oxygen and 9 for fluorine). F-18 is an unstable radioisotope and has a half-life of 109 minutes. It decays by beta-plus emission or electron capture and emits a neutrino (ν) and a positron (β^+):

$$\text{F-18} \rightarrow \text{O-18} + \beta^+ + \nu. \quad (2)$$

The positron annihilates with an electron to release energy in the form of coincident photons (Fig 1):

$$\beta^+ + e^- \xrightarrow{\text{annihilation reaction}} 0.511\text{-MeV } \gamma + 0.511\text{-MeV } \gamma. \quad (3)$$

By changing the molecule in the target chamber, other positron-emitting radionuclides such as C-11, nitrogen-13, and O-15 can be produced.

Typically, 0.3 mL of O-18–enriched water in a silver container (called a *slug*) is the target for production of 400–500 mCi of F-18 under standard conditions by using the cyclotron at our institution. This process takes approximately 20 minutes. By varying the amount of O-18–enriched water in the slug, larger quantities of F-18 fluoride can be produced.

Synthesis of FDG

Bombarding O-18–enriched water with protons in the cyclotron results in a mixture of H_2(F-18) and O-18–enriched water. Synthesis of FDG from this mixture is an automated computer-controlled radiochemical process (12) that takes approximately 50 minutes to complete. The FDG thus produced is a sterile, nonpyrogenic, colorless, and clear liquid, with residual solvent of less than 0.04%. The radioactive purity is greater than 95%, and the residual activity is approximately one-third to one-half of the original activity (which may vary depending on the synthesis process).

FDG PET Imaging

Tumor Physiology and FDG Uptake

The hallmarks of malignant cells are rapid proliferation, increase in size, local invasion, and distant metastasis. Tumorigenesis is supported by numerous polypeptide growth factors (platelet-derived growth factor [PDGF] and insulin-like growth factor) and factors promoting tumor angiogenesis (vascular endothelial growth factor [VEGF] and basic fibroblast growth factor [bFGF]) (13). Rapidly proliferating large tumors outgrow their vascular supply, resulting in ischemia and necrosis of the tumor. One to 2 mm is the limit of enlargement of tumor diameter beyond which vascularization is needed for further tumor growth, the 2-mm size limit representing maximal oxygen and nutrients diffusing distance capability from blood vessels (13).

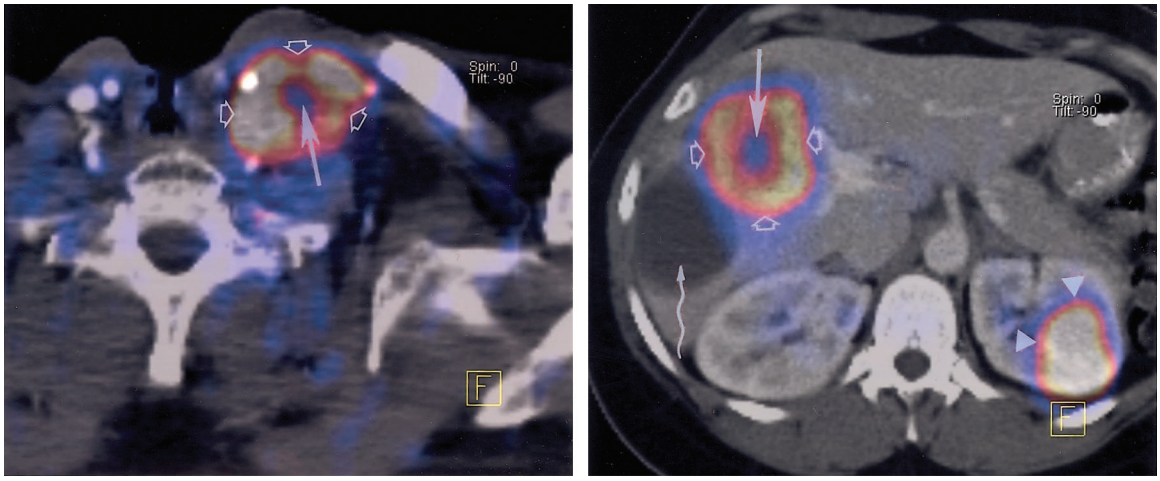

a. **b.**

Figure 4. Differential uptake of FDG. Axial fused FDG PET–CT images of patients with supraglottic squamous cell carcinoma **(a)** and colon cancer **(b)** show metastases to a left supraclavicular lymph node **(a)** and to the liver **(b)**. The metastases demonstrate differential FDG uptake in proportion to their metabolic activity. The necrotic centers of the metastases (straight solid arrow) show negligible uptake compared with their hypermetabolic peripheries (open arrows). Arrowheads in **b** = physiologic FDG activity in the left kidney, wavy arrow in **b** = simple hepatic cyst without metabolic activity.

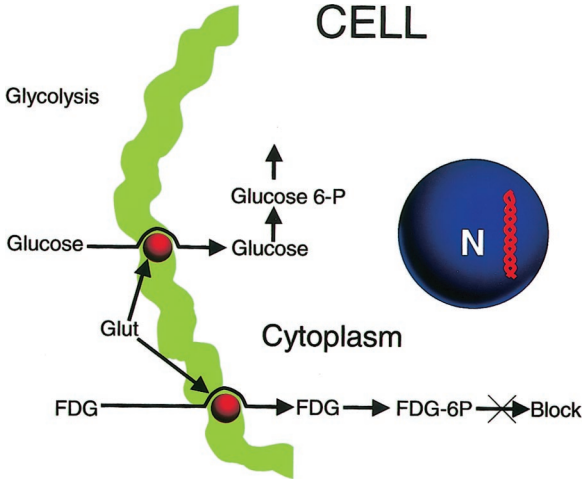

Figure 3. Uptake of FDG. FDG is a glucose analog that is taken up by metabolically active cells by means of facilitated transport via glucose transporters *(Glut)* in the cell membrane. In the cell cytoplasm, FDG undergoes phosphorylation to form FDG-6-phosphate *(6P)*, which, unlike glucose, cannot undergo further metabolism and becomes trapped within the cell. *N* = nucleus.

Malignant cells have increased glucose utilization due to upregulation of hexokinase activity (14). Glucose is taken up by tumor cells by facilitated transport (via glucose transporters [GLUT]) and then undergoes glycolysis (Fig 3) with the formation of pyruvate under aerobic conditions. However, under hypoxic conditions (in a necrotic tumor), glucose is metabolized under anaerobic conditions with resultant increased tumor lactate levels. FDG is a radiopharmaceutical analog of glucose that is taken up by metabolically active tumor cells using facilitated transport similar to that used by glucose (Fig 3). The rate of uptake of FDG by the tumor cells is proportional to their metabolic activity (Fig 4). Like glucose, it undergoes phosphorylation to form FDG-6-phosphate; however, unlike glucose, it does not undergo further metabolism, thereby becoming trapped in metabolically active cells.

Detection of Emission

A positron is a positively charged electron with the same mass as an electron that annihilates with an electron within milliseconds of its emission, releasing two photons (511 keV) moving in opposite directions. These annihilation photons, and not positrons, are detected during PET. The detectors in PET scanners are scintillation crystals coupled to photomultiplier tubes (PMTs). Compared with most radioisotopes used in nuclear medicine, the radionuclides in PET emit photons of much higher energies (511 keV for FDG vs 140 keV for technetium-99m). Hence, detectors with much higher stopping power are required.

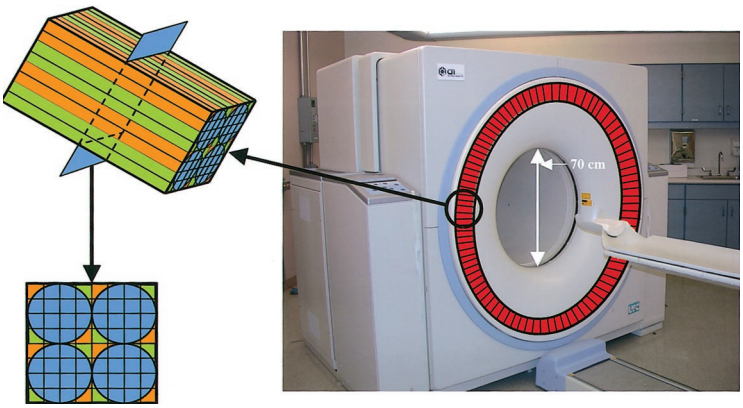

Figure 5. Photograph (frontal view) of a hybrid PET-CT scanner shows the PET ring detector system (red ring). There are up to 250 block detectors in the ring. Drawing shows a detector block with 8 × 8 smaller scintillation crystals (green and orange rectangles) linked to four photomultiplier tubes (blue circles).

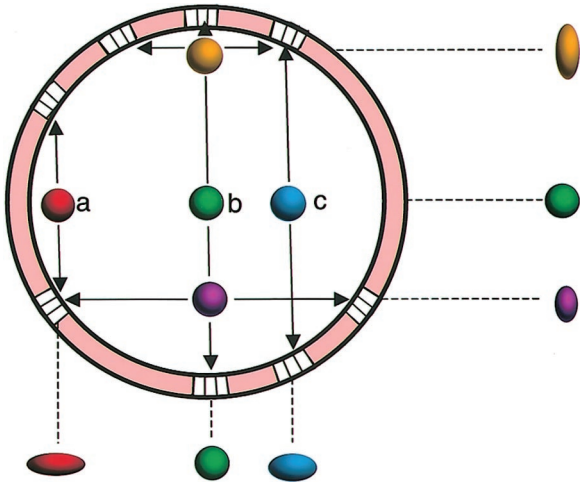

Figure 6. Radial blurring. The ring geometry of block detectors results in radial blurring due to nonuniform penetration of the detector elements by the coincidence photons. In more peripheral regions of the gantry (*a*, *c*), the annihilation photons may penetrate more than a single detector due to their oblique paths, thereby resulting in blurring of the final image. The degree of blurring is variable and depends on the obliquity of the paths of the photons through the detectors. Radial blurring is typically worse at the periphery of an image.

Most current PET scanners use crystals composed of bismuth germinate (BGO), cerium-doped lutetium oxyorthosilicate (LSO), or cerium-doped gadolinium silicate (GSO), which have very high densities and atomic numbers. The coincidence detection efficiency for 25-mm LSO or BGO crystals is approximately 80% for photons with an energy of 511 keV (15). The absorption efficiency of BGO crystals is greater than that of LSO crystals due to its higher effective atomic number; however, LSO crystals emit fivefold as much light as BGO crystals, and the decay time for LSO is lower at 40 nsec compared with 300 nsec for BGO. This enables the necessary counts or scintillation events required for image formation to be obtained in less time when LSO crystals are used, thereby significantly decreasing the scanning time and increasing patient throughput. GSO has a lower effective atomic number than BGO and LSO crystals. It can detect gamma rays across a wide energy spectrum from low-energy 28–35-keV photons from iodine-125 to 511-keV annihilation photons from FDG. GSO crystals emit slightly more light than BGO and have a decay time of approximately 50 nsec.

The BGO, LSO, or GSO scintillation crystals are made into block detectors as described by Casey and Nutt (16) in 1986. Block detectors are solid scintillation crystals into which channels are cut that are then filled with opaque material. Each detector is coupled to four photomultiplier tubes, and they are arranged in a ring geometry with as many as 250 blocks in a ring (Fig 5). The advantage of such a system over a single large crystal is that each detector in the block detector system acts as a small independent system with a decrease in the detector dead time (15). The PET scanner at our institution combines a BGO block detector (crystal size 4.05 × 4.39 × 30 mm) PET camera with the detector modules arranged in a complete ring (Fig 5). A disadvantage of the ring detector system is radial blurring, which occurs because the length of the detectors is much greater than their width (the length needs to be increased to retain their absorption efficiency) and photons close to the edge of the field of view may penetrate more than one crystal before being detected (Fig 6).

Positrons emitted from a radionuclide have enough kinetic energy to travel a small distance called the *mean positron range* (Fig 7) before annihilating with an electron. The distance is smaller in dense structures such as bone but larger for the lungs and air; for example, for FDG in water, the mean positron range is 1.4 mm (15). This change in position between the origin of the positron and its site of annihilation results in positron range blurring, limiting the spatial resolution of PET (typically 5 mm on current scanners). Another source of decreased spatial resolution is noncolinearity. When positrons and electrons annihilate, they are in motion, and the actual angle between the photons thus emitted is not exactly 180° (Fig 7). A coincidence line defines the path of the two 511-keV annihilation photons emitted. A random unpredictable variation of 0.5° from the expected 180° is observed. Because an exact 180° angle between the photons is assumed during image reconstruction, the small variation of 0.5° causes an additional decrease in spatial resolution called *annihilation angle blurring*. The magnitude of this error increases with an increase in the distance between the two detectors detecting the coincident events; it can therefore be decreased by reducing the diameter of the scanner.

The 511-keV photons emitted opposite to each other easily penetrate soft tissues. The point of annihilation of a positron is not necessarily equidistant from the detector ring for both annihilation photons; therefore, although two photons may be coincident, they might not be detected at the same time by two detectors (Fig 8). For this reason, photons interacting with detectors within a set time window are considered to be "in coincidence." The window for this coincidence detection is typically 6–12 nsec. Photons outside this time window are considered as single events and discarded by the coincidence circuit—as many as 99% of the photons detected may be rejected. This "electronic collimation" via coincidence detection (15) makes PET much more efficient than other nuclear medicine procedures. However, the detection and processing of annihilation photons that will never have a corresponding coincident count contribute to the dead time.

When two photons from an annihilation reaction reach the detectors within the required time window for a coincidence count but one of the photons has scattered (change of direction and loss of energy) before reaching the detector, the coincidence line no longer passes through the point of annihilation. These errors due to scattered counts result in decreased resolution and are corrected by subtracting the estimated scattered counts from the observed counts. Random counts, an additional source of noise, are events from different annihilation reactions that are detected within the same time window. If two separate single events reach the detectors within the time window for a coincidence count, then they will falsely be considered to be in coincidence; however, the coincidence line will not contain the point of annihilation of either event.

In addition to electronic collimation, two thick rings of lead collimators are placed in front of and behind the plane of the detector ring to reduce the possibility of annihilation photons from body parts outside the scanner reaching the scintillation crystals for three-dimensional PET studies. In contrast, with two-dimensional PET, additional multiple septa capable of stopping the high-energy photons are positioned between the patient and the scintillation crystal, thereby reducing the scatter but decreasing the geometric sensitivity.

PET-CT Fusion

PET is limited by poor anatomic detail, and correlation with some other form of imaging, such as CT, is desirable for differentiating normal from abnormal radiotracer uptake. Beyer et al (11) described the prototype PET-CT scanner used in clinical imaging, in which precisely coregistered functional and anatomic images can be obtained by performing a PET study and a CT study on the same scanner without moving the patient. At our institution, we have a hybrid PET-CT scanner (CTI PET Systems, Knoxville, Tenn) that is a combination of an ECAT EXACT HR+ PET scanner (Siemens Medical Solutions, Erlangen, Germany) and a single-row helical SOMATOM Emotion CT scanner (Siemens Medical Solutions) with ceramic detector elements (17) housed back-to-back (Fig 9). This scanner maintains mechanical isolation between the PET and CT components (17), unlike the prototype partial-ring scanner (11), in which the PET and CT hardware were on the same gantry. The gantry aperture is uniform over the PET and CT components and is 70 cm (versus 60 cm on the prototype). The CT unit is a subsecond helical scanner with minimum and maximum full rotation times of 0.8 and 1.5 seconds, respectively, and in-plane spatial resolution of 0.32 mm (17). The function and capability of the scanner are similar to those of the stand-alone CT system; the only difference is that the gantry of the CT scanner has no tilt capability.

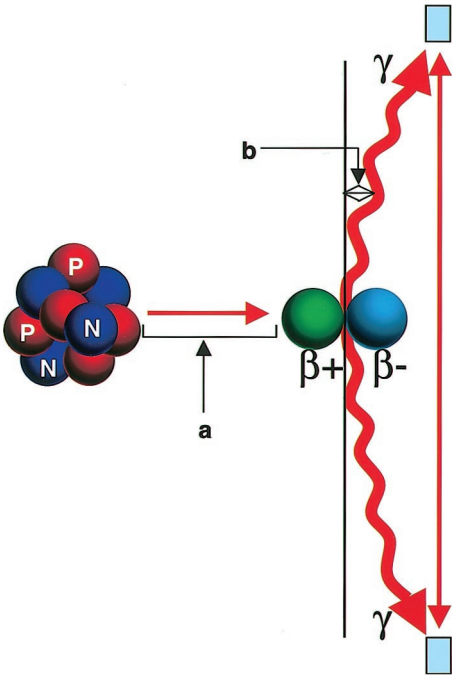

Figure 7. Mean positron range and annihilation angle blurring. Positrons (β+) travel a small distance called the *mean positron range (a)* before annihilating with electrons (β−). This change in position between the origin of the positron and its site of annihilation results in positron range blurring, thus limiting the spatial localization that can be achieved with PET. In addition, positrons and electrons are in motion when they annihilate; therefore, the annihilation photons (γ) are not at exactly 180° to each other. The unpredictable 0.5° variation *(b)* between the annihilation photons results in additional spatial degradation, which is called *annihilation angle blurring*. *N* = neutron, *P* = proton.

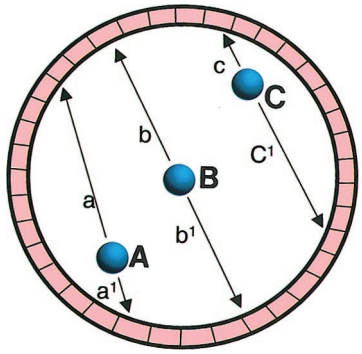

Figure 8. Coincidence imaging. Although the photons emitted by annihilation points *A* and *C* are in coincidence, the distances that the coincident photons *a* and a^1 and *c* and c^1 will travel before they reach the scintillation crystals are different. There is a predetermined time window within which detected photons are considered to be in coincidence. Therefore, even though photons *a* and a^1 and *c* and c^1 are coincident, they will be electronically rejected as noncoincident. However, the coincident photons from point *B* are likely to reach the scintillation crystals within the time window and will be accepted as coincident.

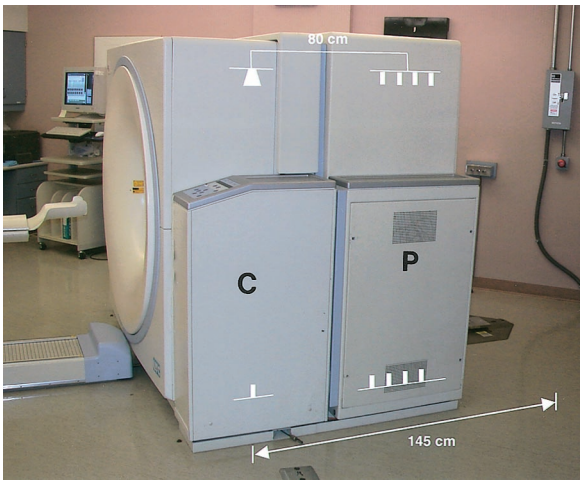

Figure 9. Photograph (side view) of a hybrid PET-CT scanner shows the PET *(P)* and CT *(C)* components. The distance between the PET and CT scanners is 80 cm, and the maximum coverage that can be achieved during a combined study is 145 cm. The PET and CT scanners are mechanically independent and can be used in isolation for PET or CT only.

Scanning Technique

Patient Preparation

Patients are required to fast for approximately 4–6 hours prior to PET-CT to enhance FDG uptake by tumors as well as to minimize cardiac uptake. They are instructed to avoid caffeinated or alcoholic beverages but can have water during this period. Before injection of FDG, the blood glucose level is measured; a level of less than 150 mg/dL is desirable. Good control of blood glucose is essential because the uptake of FDG into cells is competitively inhibited by glucose, as they use a common transport mechanism (glucose transporters [GLUT]) for facilitated transport into both normal and tumor cells. There is lack of agreement as to administration of insulin in diabetic patients for glucose control. Insulin facilitates transfer of glucose into muscle, adipose, and several other tissues (except brain and liver tissue, which do not require insulin for efficient glucose uptake) via GLUT, and the administration of insulin for glucose control in diabetics may exaggerate physiologic uptake in muscles. Patients are also instructed to avoid any kind of strenuous activity prior to the examination and following injection of the radioisotope to avoid physiologic muscle uptake of FDG.

Bowel cleansing, advocated by certain authors during PET (18), is not used prior to PET-CT at our institution. There is a lack of consensus regarding bladder catheterization during PET. At our institution, urinary bladder catheterization is tailored according to each patient's clinical history (Fig 10). All oncology patients with the exception of those being studied for head and neck malignancy are given water-soluble iodinated contrast media orally for bowel opacification.

The typical dose of FDG is 10 mCi injected intravenously. Patient activity and speech are limited for 20 minutes immediately following injection of the radioisotope to minimize physiologic uptake by muscles. To our knowledge, there are no contraindications to FDG administration. Imaging is initiated approximately 60 minutes following the injection of FDG. Patients undergo catheterization if necessary, or they void just before being positioned on the PET-CT table. They are positioned either with the arms above the head or with the arms at the side. Except for patients being studied for head and neck cancer, arms above the head is the preferred position to decrease beam-hardening artifact during the CT portion of the examination. However, not all patients can maintain this position comfortably without moving for the entire study (PET and CT), and arms by the side is an alternative. A whole-body PET study (neck through pelvis) follows an enhanced whole-body CT study. The CT study takes approximately 60–70 seconds to complete and the PET study takes approximately 30–45 minutes, depending on the coverage required.

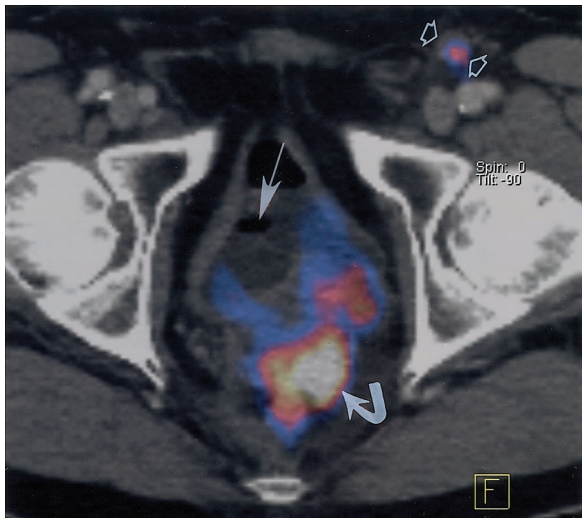

Figure 10. Recurrent colorectal carcinoma in a 65-year-old man after surgical resection. FDG PET–CT was performed to evaluate for recurrence. Axial fused FDG PET–CT image of the pelvis shows a Foley catheter in the urinary bladder (straight solid arrow). Recurrent disease in the pelvis (curved arrow) may be obscured by an FDG-distended bladder if catheterization is not used. Open arrows = metastatic left inguinal lymph node.

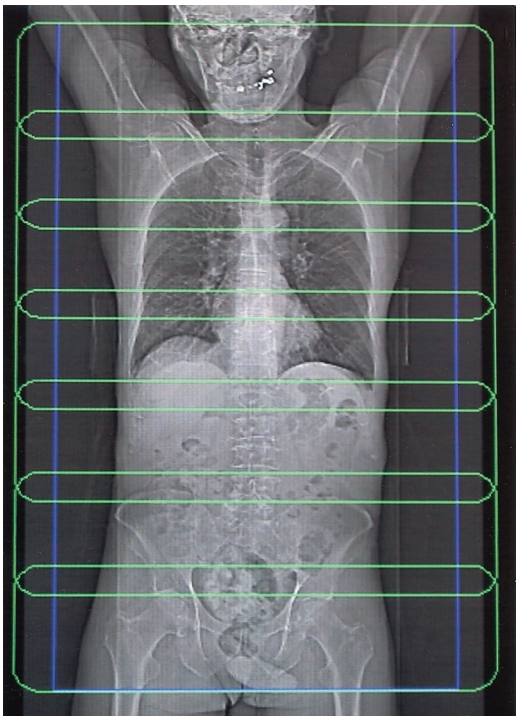

Figure 11. Typical scout image obtained during an FDG PET–CT study. The blue-purple rectangle represents CT coverage during the study, and each overlapping green rectangle represents PET coverage. Six to seven bed positions are required for PET coverage of the neck, chest, abdomen, and pelvis.

CT Technique

Single-phase contrast material–enhanced helical CT is performed following injection of 125 mL of a low-osmolarity iodinated contrast medium (ioversol; Optiray 350, Mallinckrodt, St Louis, Mo) at a rate of 4 mL/sec by using a power injector (Medrad, Indianola, Pa). For a typical whole-body PET-CT study (neck, chest, abdomen, and pelvis), scanning begins at the level of the skull base and extends caudally to the level of the symphysis pubis (Fig 11). The total length of CT coverage is an integral number of bed positions scanned during acquisition of PET data. The study is performed with the patient breathing quietly. Typical scanning parameters would be a collimator width of 5.0 mm, pitch of 1.5, gantry rotation time of 0.8 second, and field of view of 50 cm. The helical data are retrospectively reconstructed at 2.4-mm intervals.

PET Technique

The PET scanner is located behind the CT scanner and housed in the same extended-length gantry. PET is performed following the CT study without moving the patient. Approximately six to seven bed positions are planned in the three-dimensional acquisition mode for scanning the entire patient (Fig 11) with 5–7-minute acquisition at each bed position. The maximum length of the patient that can be scanned with the current PET-CT scanner is 145 cm (Fig 9) compared with 100 cm on the prototype (17). Each bed position (in the craniocaudal direction) is 15.5 cm long, and the table moves 11.5 cm following acquisition of data at each bed position—there is approximately a 4-cm (~25%) overlap between table stations. The field of view is 58.5 cm, the spatial resolution is approximately 5 mm, and the sections are postprocessed to a thickness of 2.4 mm for fusion with CT images.

Interpretation of Images

PET provides images of quantitative uptake of the radionuclide injected that can give the concentration of radiotracer activity in kilobecquerels per milliliter. However, for accurate results, the images must be corrected for effects of attenuation of the 511-keV photons as they pass through the patient. In contrast to PET, which used an external radioactive transmission scan, PET-CT uses CT transmission data to correct for attenuation differences. After reconstruction, the CT, attenuation-corrected, and attenuation-uncorrected images obtained from the unified PET and CT protocol are transferred to, integrated at, and displayed on the syngo software platform (Siemens Medical Solutions). Differential PET to CT weighting, crosshairs linking of the axial, coronal, and sagittal reformatted images, and interactive viewing of the CT, PET, and fused images are possible (Fig 12).

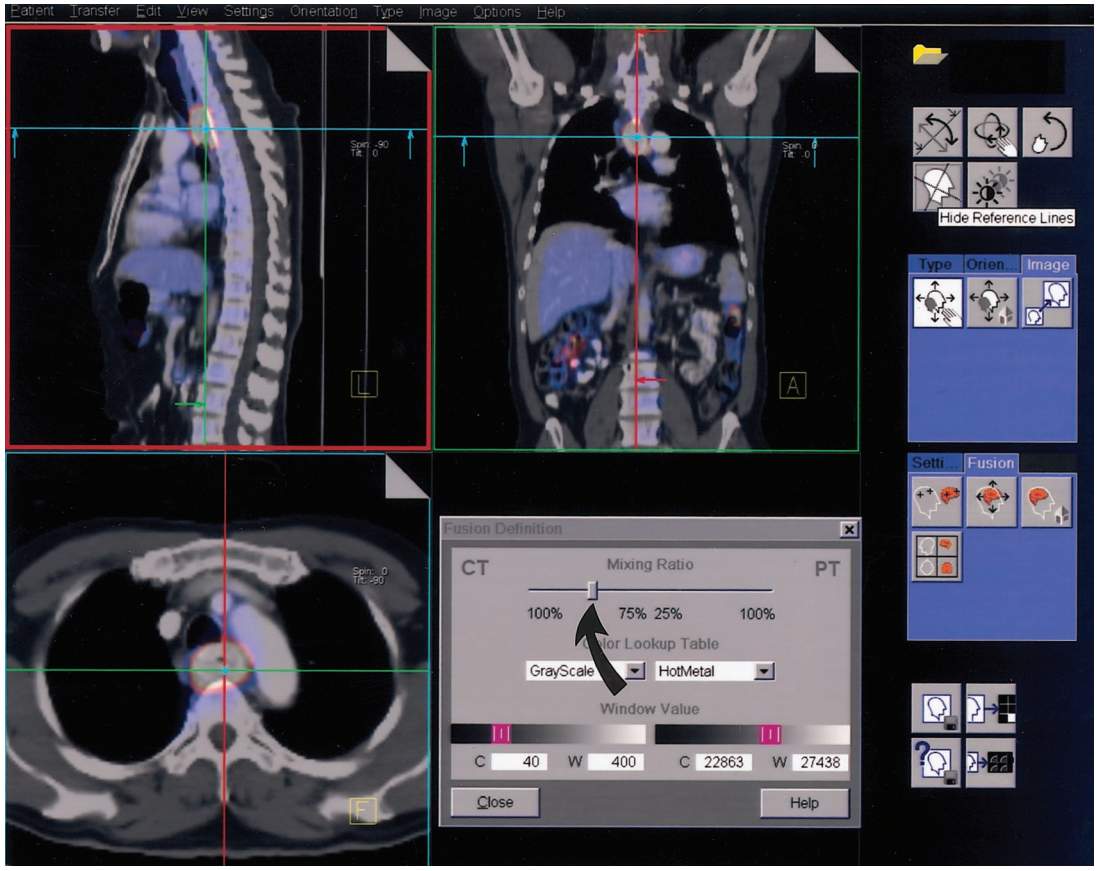

Figure 12. Display screen of the syngo software platform shows fused PET-CT images in the sagittal, coronal, and axial planes of a patient with recurrent esophageal carcinoma. Placing the crosshairs on the tumor automatically coregisters it in all three orthogonal planes. By dragging the vertical bar (arrow) along the horizontal line in the lower right quadrant of the screen, the PET and CT weighting of the image can be altered. In this image, the CT to PET ratio is 75% to 25%.

There are different methods for assessment of radiotracer uptake by normal and pathologic tissues, such as visual inspection, the standardized uptake value (SUV), and the glucose metabolic rate. We most frequently use visual inspection in analysis of PET-CT results by comparing PET and CT data, as well as viewing fused PET-CT images. SUVs are used for semiquantification of FDG uptake. Another method of quantification of dynamic PET results is the more complex glucose metabolic rate calculation.

Standardized Uptake Value

The SUV is a semiquantitative assessment of the radiotracer uptake from a static (single point in time) PET image. The SUV of a given tissue is calculated with the following formula:

$$\frac{\textit{tracer activity in tissue}}{\textit{injected radiotracer dose/patient weight}}, \quad (4)$$

where tissue tracer activity is in microcuries per gram, injected radiotracer dose is in millicuries, and patient weight is in kilograms. The SUV of a tissue can be depicted as the minimum, maximum, or mean in the region of interest. The mean SUV is the mathematical mean of all the pixels in the region of interest, whereas the minimum and maximum SUV are values of the pixel with the lowest and highest SUV, respectively. We rely on visual inspection and use SUV in assessing questionable lesions or in the follow-up of FDG-avid masses. Typically, malignant tumors have an SUV of greater than 2.5–3.0, whereas normal tissues such as the liver, lung, and marrow have SUVs ranging from 0.5 to 2.5. Variations in the SUV have been described such as the glucose-corrected SUV and SUV normalized by surface area or lean body mass. It is useful to know the tumor SUV before initiation of therapy to assess tumor grade and evaluate treatment response following radiation therapy or chemotherapy (15). It is important to standardize the time interval be-

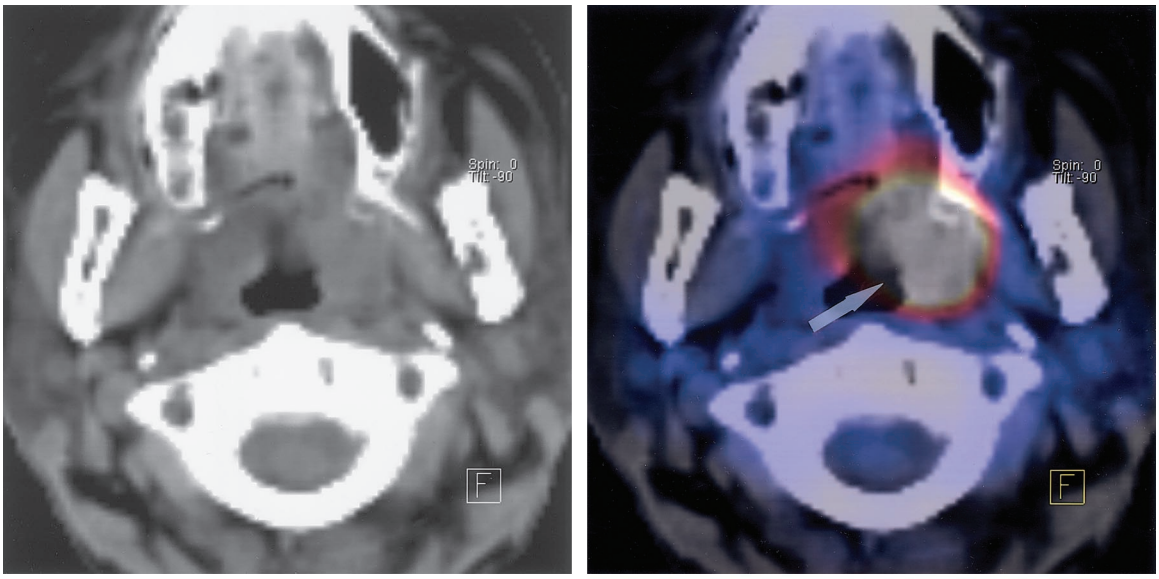

a. b.

Figure 13. Metastatic squamous cell carcinoma in a 45-year-old woman. After biopsy of a right cervical lymph node revealed the carcinoma, FDG PET–CT was performed to search for the primary tumor. **(a)** Axial CT image obtained at the level of the oropharynx shows mild tonsillar asymmetry without a definite mass. **(b)** Corresponding fused FDG PET–CT image shows intense hypermetabolism in the left tonsil (arrow), which was the site of the primary tumor.

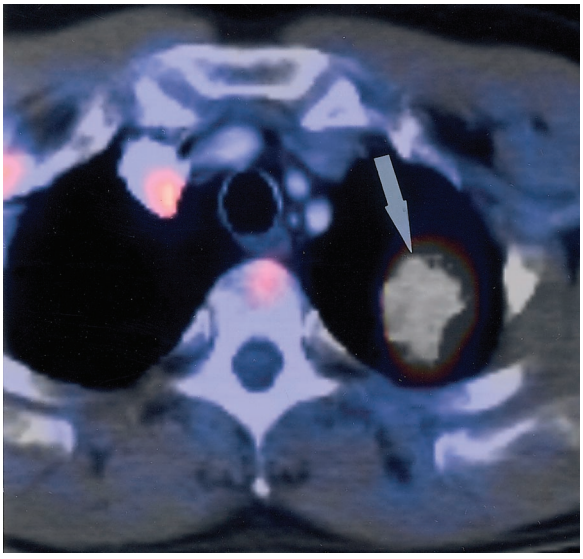

Figure 14. Adenocarcinoma in a 50-year-old man with a mass in the apex of the left lung. Results of multiple biopsies were negative for malignancy. FDG PET–CT was performed for further characterization of the mass. Axial fused FDG PET–CT image shows marked hypermetabolism in the lesion (arrow), which proved to be a poorly differentiated adenocarcinoma at subsequent left upper lobectomy.

tween injection of the radiotracer and the PET study because SUV variability with time has been well documented (19).

Clinical Applications in Oncology

Cancer is one of the leading causes of morbidity and mortality in developed countries such as the United States. Various imaging modalities based on anatomic information continue to be important for the diagnosis and in the follow-up of oncologic disease; however, they have a notable limitation of not allowing detection of morphologically normal but functionally abnormal tissues. The functional and anatomic information offered by PET-CT is being recognized as crucial in the care of oncology patients. PET (20) and PET-CT are playing an ever-increasing role in the management of oncologic disease. They have been accepted in the diagnosis, staging, and follow-up of non–small cell lung cancer, lymphoma, colorectal and esophageal cancer, melanoma, head and neck cancers, and breast cancer and for characterization of solitary pulmonary nodules. Illustrative examples show the usefulness of PET-CT in the diagnosis (Figs 13–16) and staging (Figs 17–19) of malignancy as well as in directing intervention (Figs 19, 20) and follow-up (Figs 21–25) of such patients.

Figures 15, 16. **(15)** Laryngeal carcinoma in an 80-year-old man who underwent FDG PET–CT to characterize a new pulmonary nodule in the left upper lobe. **(a)** Axial fused FDG PET–CT image of the pulmonary nodule shows intense hypermetabolism (arrow), which was due to metastatic squamous cell carcinoma at wedge resection. **(b)** Axial CT image of the neck shows nonspecific bilateral thyroid nodules (solid arrows) with foci of calcification (open arrows), which were incidentally noted and are suggestive of multinodular goiter. **(c)** Corresponding fused FDG PET–CT image shows intense hypermetabolism in the left-sided thyroid nodule (curved arrow). Total thyroidectomy revealed left-sided papillary thyroid carcinoma and right-sided multinodular goiter. Open arrows = foci of calcification. **(16)** Biopsy-proved poorly differentiated non–small cell carcinoma in the native left lung in a 56-year-old man with idiopathic pulmonary fibrosis and a right lung transplant. **(a)** Axial CT image shows a large, conglomerate pulmonary mass in the left lower lobe (straight arrow) with enlargement of a subcarinal lymph node (curved arrow). **(b)** Corresponding fused FDG PET–CT image shows intense hypermetabolism in the mass (straight arrow) and the metastatic node (curved arrow).

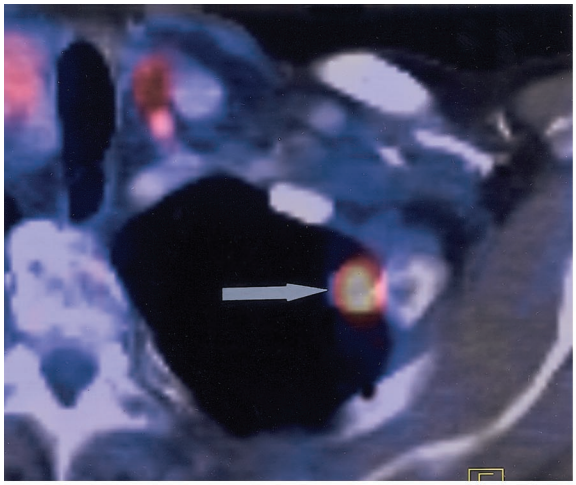

15a.

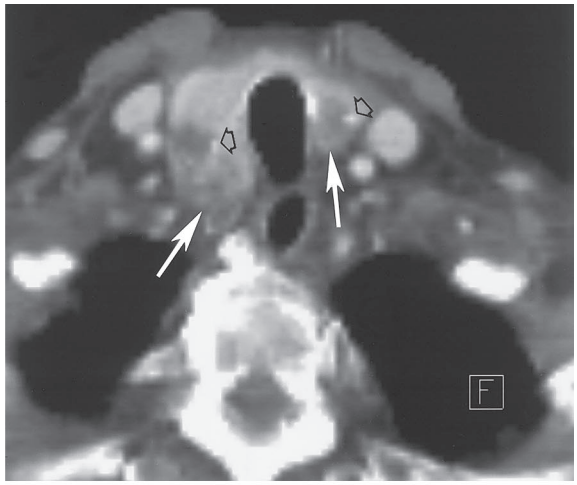

15b.

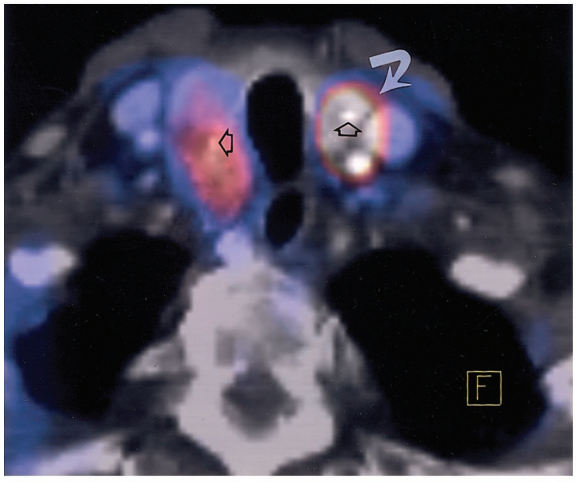

15c.

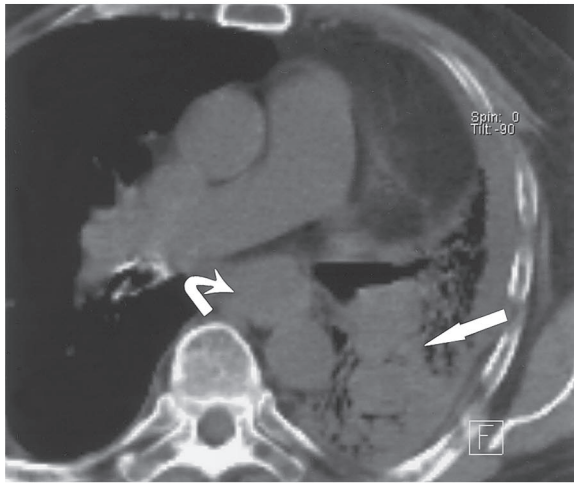

16a.

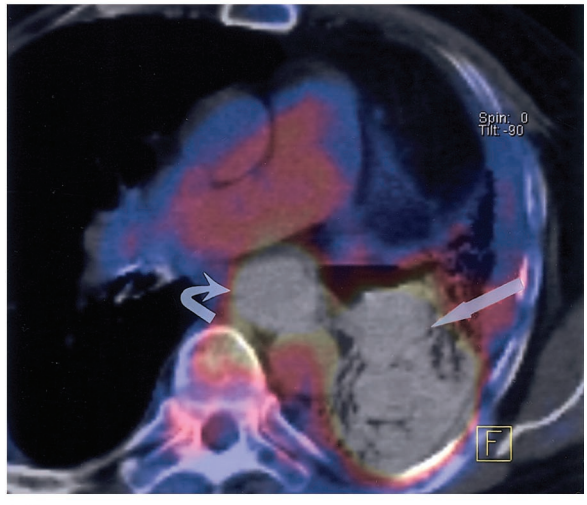

16b.

Figures 17–20. **(17)** Melanoma in a 33-year-old man. The extent of disease was evaluated with FDG PET–CT. Axial **(a)** and sagittal **(b)** fused FDG PET–CT images show focal hypermetabolism in the left paraspinal soft tissue (arrow in **a**) and in T8 (arrow in **b**), findings consistent with metastases. CT showed only subtle areas of decreased attenuation. Arrowheads in **a** = misregistration artifact due to cardiac motion. **(18)** Non–small cell lung carcinoma in a 78-year-old man with enlarged hilar and mediastinal lymph nodes. FDG PET–CT was performed for staging. Axial fused FDG PET–CT image shows an enlarged subcarinal node without abnormal metabolism (straight arrow), which was reactive. The metastatic left hilar node is FDG avid (wavy arrow), as was the primary tumor. **(19)** Large B-cell lymphoma in a 74-year-old man. FDG PET–CT was performed for staging. Sagittal fused FDG PET–CT image shows wedge compression deformity of L4 with moderate hypermetabolism (arrow), which was confirmed at biopsy to be metastasis. **(20)** Large cell lung cancer in a 54-year-old woman. Axial fused FDG PET–CT image shows hypermetabolism within a lung mass (arrow) and distal drowned lung (arrowheads). Precise localization of a tumor within a larger mass helps direct intervention such as biopsy.

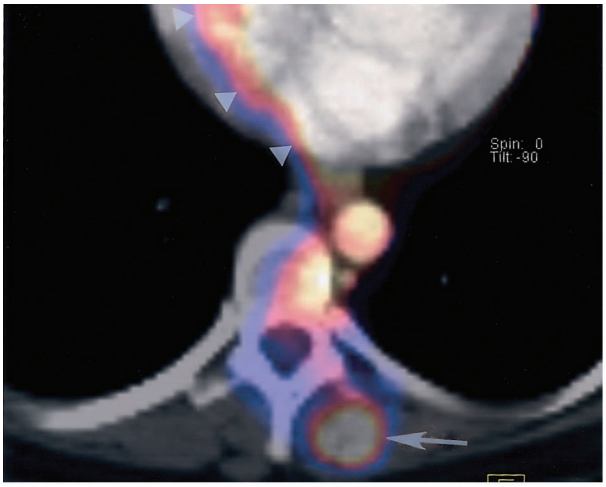

17a.

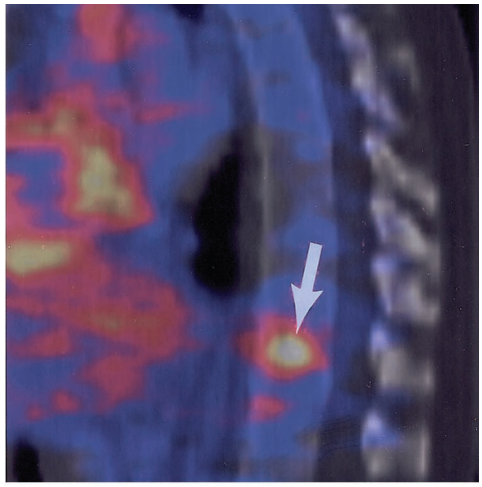

17b.

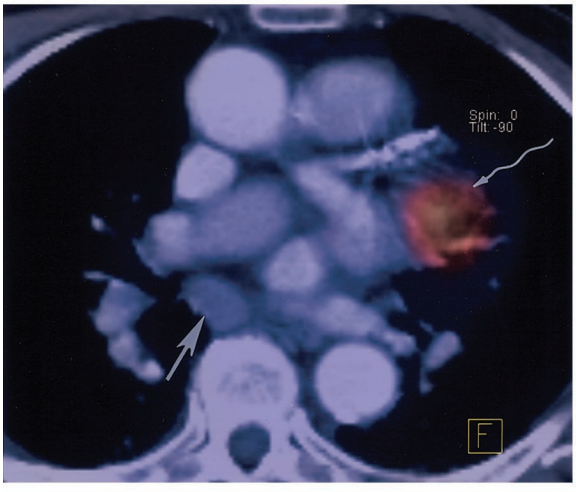

18.

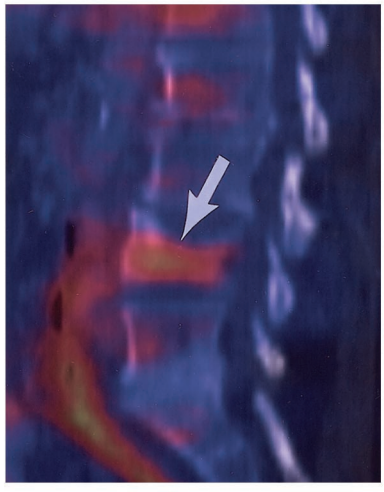

19.

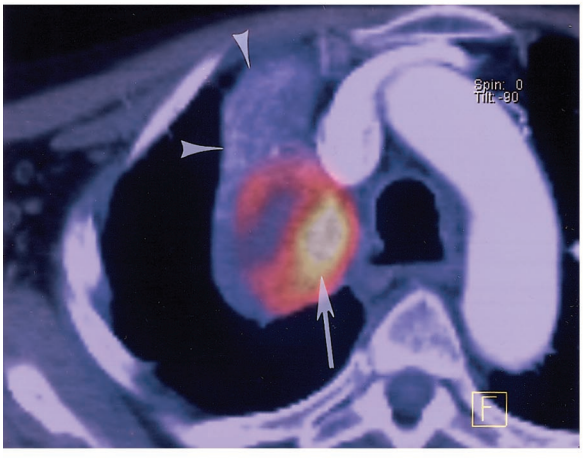

20.

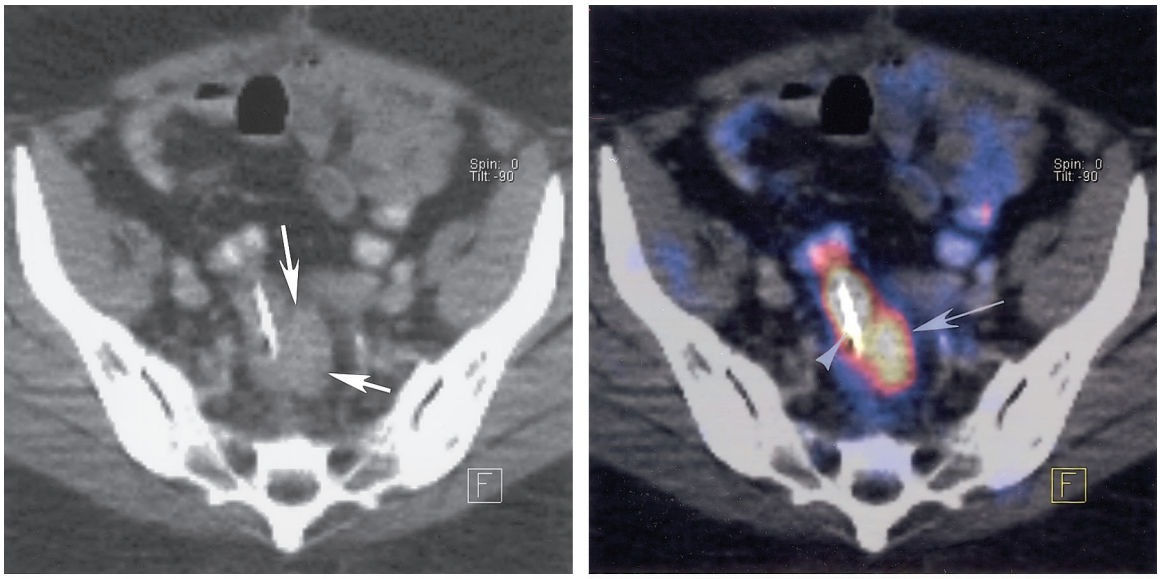

a. **b.**

Figure 21. Recurrent colorectal carcinoma in a 55-year-old woman after surgical resection. FDG PET–CT was performed to evaluate for recurrence because of a rising level of carcinoembryonic antigen. **(a)** Axial contrast-enhanced CT image of the pelvis shows minimal presacral soft tissue at the surgical site (arrows). **(b)** Corresponding fused FDG PET–CT image shows intense hypermetabolism at the surgical site (arrow), which was due to local recurrence. Arrowhead = suture from surgery.

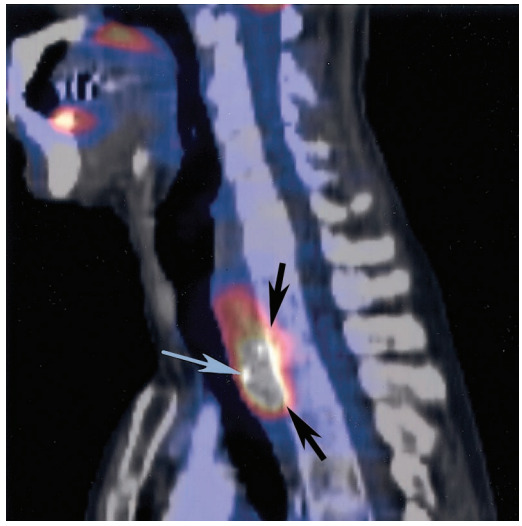

Figure 22. Recurrent esophageal carcinoma in a 63-year-old man after surgical resection. Follow-up CT showed an enlarging soft-tissue mass at the surgical site. FDG PET–CT was performed to evaluate for recurrence. Sagittal fused FDG PET–CT image shows intense hypermetabolism at the surgical site (black arrows), thus confirming the presence of recurrent disease. White arrow = suture from surgery.

Limitations and Artifacts of PET-CT

Patient motion in PET-CT imaging can produce significant artifacts on the fused images and may cause confusion as to the correct position of the origin of the detected photon. Patients are instructed not to move for the entire study, that is, between the initial CT examination and the later PET examination, as this is extremely important for proper coregistration of the CT and PET studies, on which depends both accurate spatial localization of tracer activity and valid attenuation correction. Patient motion is minimized by *(a)* carefully instructing patients not to move during the study; *(b)* placing them in a comfortable position before the start of the study; *(c)* ensuring that they are not taking diuretics, which may otherwise require them to evacuate the bladder during the study; and *(d)* having patients empty their bladder before the start of the study

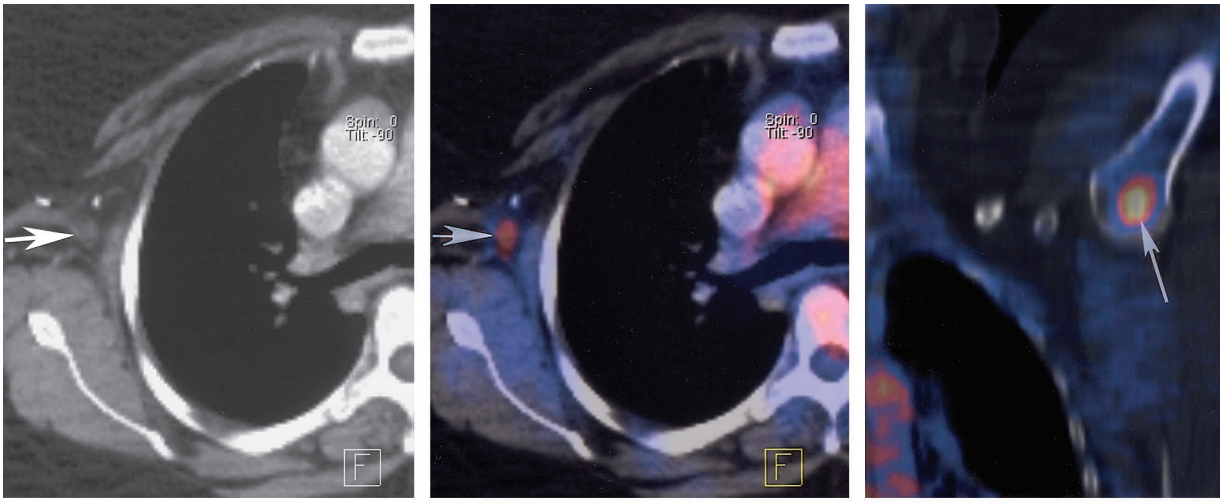

a. b. c.

Figure 23. Recurrent metastatic disease in a 33-year-old woman with invasive ductal carcinoma of the right breast, which was treated with surgical resection and dissection of the left axillary nodes. FDG PET–CT was performed to evaluate for recurrence. **(a)** Axial CT image shows a small lymph node in the right axilla (arrow). **(b)** Corresponding fused FDG PET–CT image shows mild hypermetabolism in the node (arrow), which represents recurrent metastatic disease. **(c)** Coronal fused FDG PET–CT image shows intense hypermetabolism in the left humeral head (arrow), which represents recurrent metastatic disease.

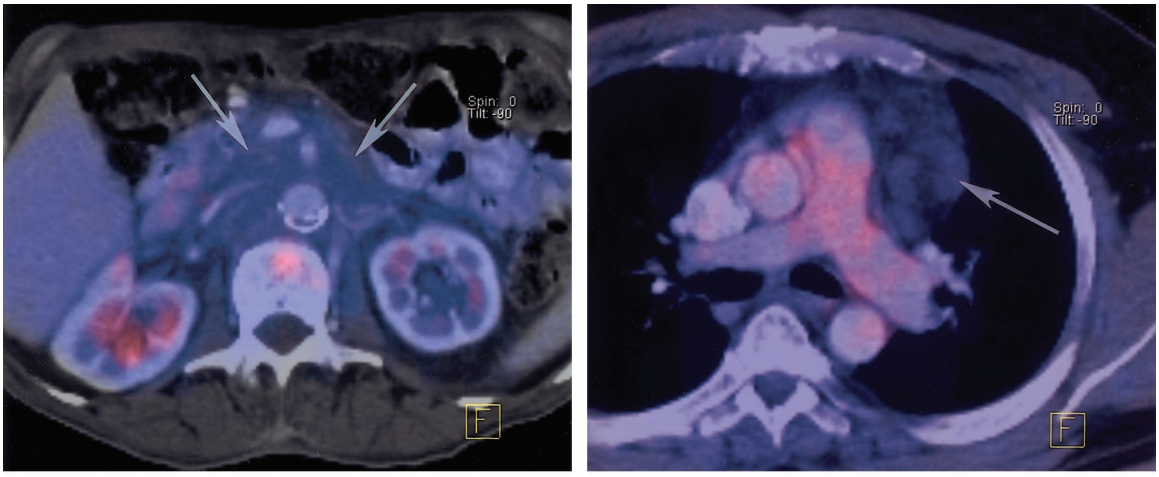

24. 25.

Figures 24, 25. **(24)** Residual fibrosis in a 40-year-old man with non-Hodgkin lymphoma, which was treated with chemotherapy. Axial fused FDG PET–CT image shows extensive thickening of periaortic and retroperitoneal soft tissue without metabolic activity (arrows), findings indicative of residual fibrosis. Follow-up FDG PET–CT images were unchanged. **(25)** Residual fibrosis in a 39-year-old man with large B-cell lymphoma. FDG PET–CT was performed for restaging after chemotherapy and radiation therapy. Axial fused FDG PET–CT image obtained at the level of the main pulmonary artery shows numerous prevascular lymph nodes—which are considered enlarged according to size criteria—with surrounding abnormal soft tissue without metabolic activity (arrow), findings indicative of residual fibrosis.

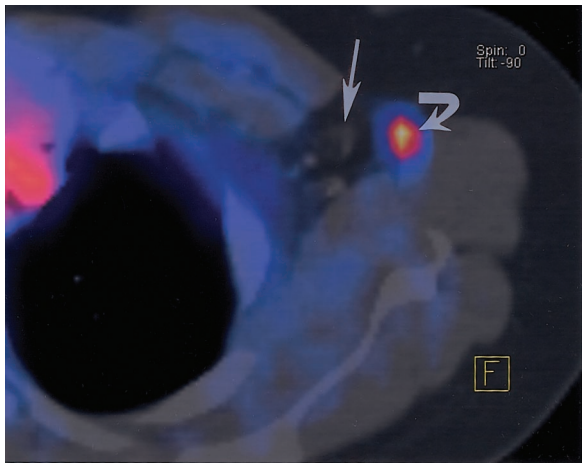

Figure 26. Misregistration artifact. FDG PET–CT was performed for staging in a patient with carcinoma of the left breast. Axial fused FDG PET–CT image shows a lymph node in the left axilla (straight arrow). Focal hypermetabolism in the node (curved arrow) appears lateral to its expected location in the axilla and overlies axillary fat instead of the node. Misregistration between the CT and PET images is due to patient motion between the CT and PET portions of the examination.

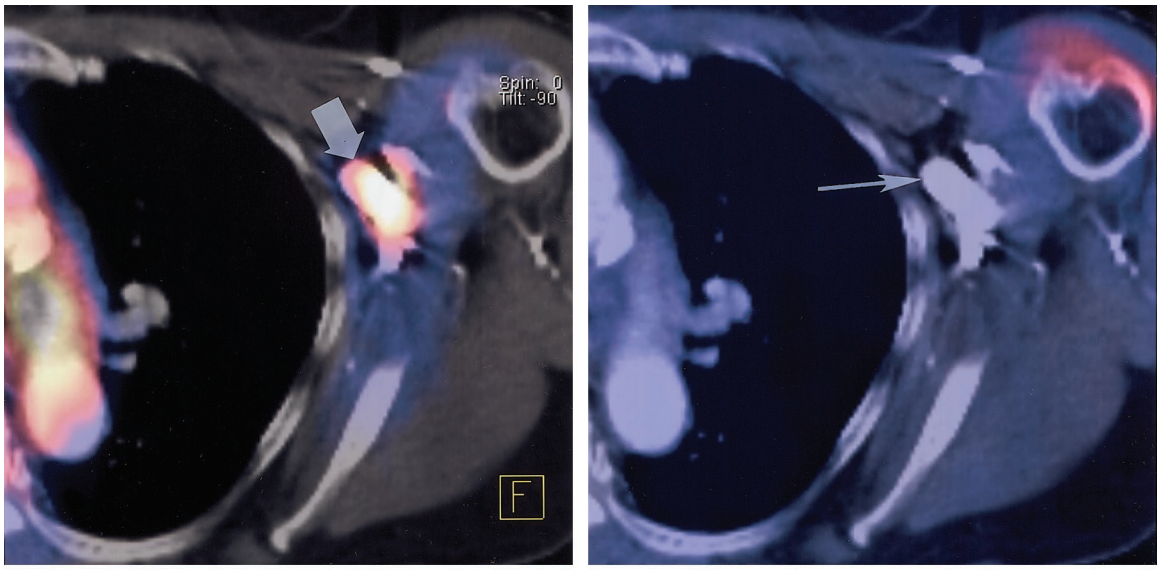

a. **b.**

Figure 27. Attenuation correction artifact. **(a)** Attenuation-corrected axial fused FDG PET–CT image shows a focus of hypermetabolism in the left axilla (arrow). **(b)** Attenuation-uncorrected fused FDG PET–CT image obtained at the same level shows lack of activity in the intensely enhancing (high-attenuation) left axillary vein (arrow), which is on the side of contrast material injection. This artifact is due to overcorrection by the attenuation correction software, which uses CT data for attenuation correction.

or catheterizing the bladder. Respiratory, cardiac (Fig 17), and bowel motion are unavoidable. Patient motion between the CT and PET studies appears as a mismatch between the two sets of images; for example, an area of increased activity in the axilla on the PET scan may not coregister exactly with an enlarged axillary lymph node (Fig 26) but may be a section above or below the lesion. By comparing the activity of the tracer over normal organs (such as the liver and kidney) and their CT images, this artifact can be recognized and the degree and direction of offset can be determined and accounted for during interpretation of the images.

Attenuation (transmission) correction artifacts can occur where there are highly attenuating objects in the path of the CT beam, such as hip prostheses, pacemakers, dental devices, and contrast-enhanced vessels (Figs 27, 28). Attenuation

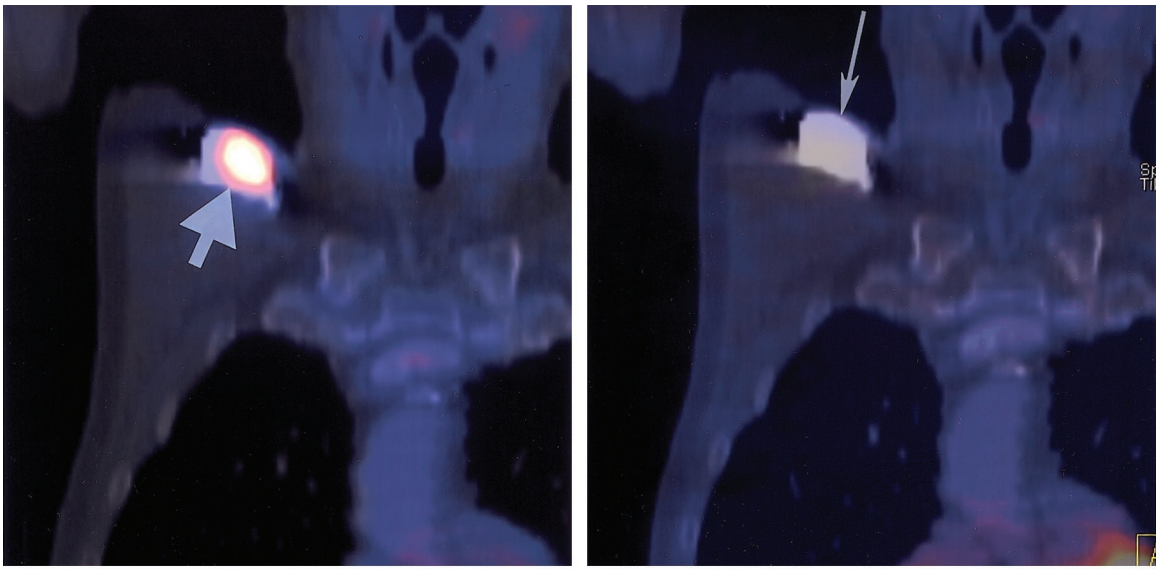

a. b.

Figure 28. Attenuation correction artifact. **(a)** Attenuation-corrected coronal fused FDG PET–CT image shows a focus of intense hypermetabolism in the right supraclavicular region (arrow). **(b)** Attenuation-uncorrected fused FDG PET–CT image obtained at the same level shows that the apparent focus of hypermetabolism is an attenuation correction artifact from a pacemaker (arrow).

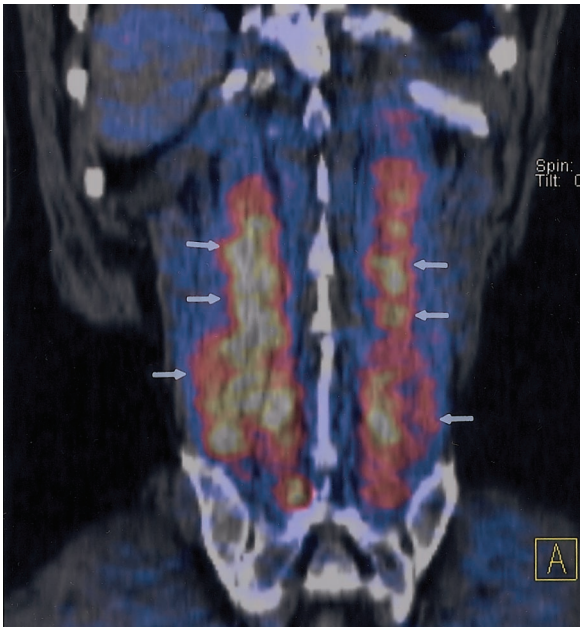

Figure 29. Physiologic muscle activity. Coronal fused FDG PET–CT image of the back shows bilateral, diffuse, symmetric moderate hypermetabolism in the paraspinal muscles (arrows). Muscular activity due to activity by the patient before or after FDG administration may result in this pattern of radiopharmaceutical uptake.

correction is required because PET is an emission scanning technique, and the fraction of photons absorbed by different body parts needs to be taken into consideration to correctly assess the activity from a given structure. PET-CT attenuation correction software corrects for absorption of photons by using the "transmission" data from CT images. It corrects (or overcorrects) photopenic areas adjacent to high-attenuation structures at CT and makes them appear hypermetabolic on the attenuation-corrected PET images. These artifacts can easily be determined by comparing the attenuation-corrected images with the uncorrected images. If the uptake adjacent to a high-attenuation structure, for example, a metal hip prosthesis, is an artifact, then the uncorrected images will show it as a photopenic region even though it may appear to have increased tracer uptake on the corrected images.

Finally, if the patient has undergone strenuous activity preceding or following injection of FDG, normal muscles may take up the radiotracer and show increased activity on the PET images (Fig 29). This is usually easy to distinguish from malignancy by comparison with the CT images for a

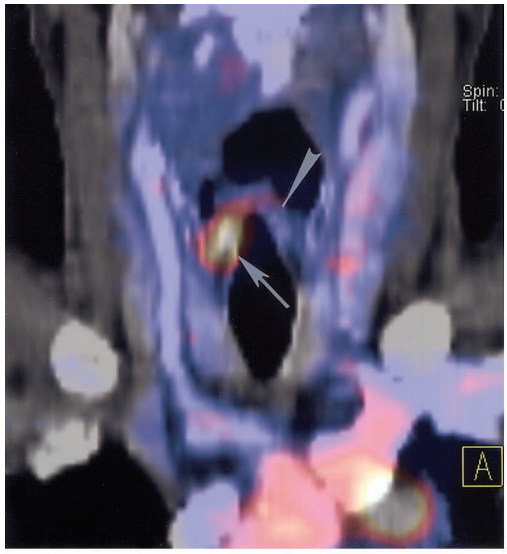

a.

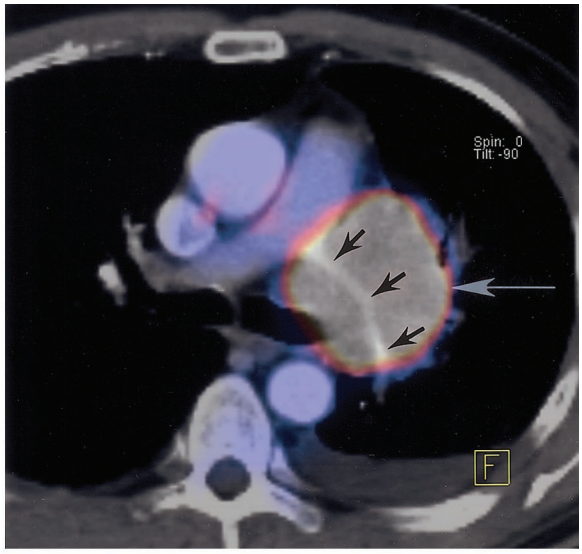

b.

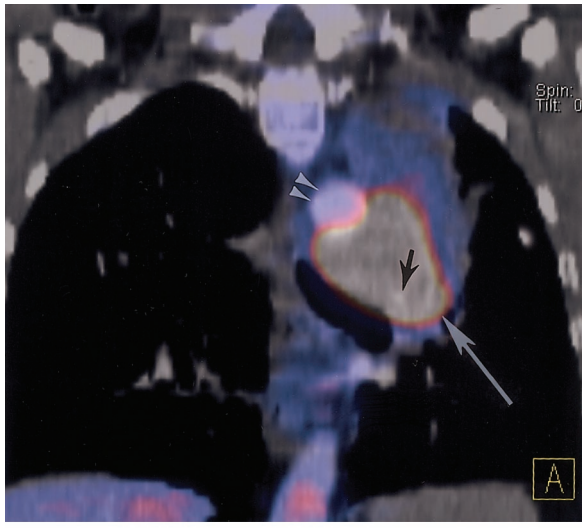

c.

Figure 30. Large cell lung carcinoma in a 64-year-old man. **(a)** Pretherapy coronal fused FDG PET–CT image of the neck shows moderate hypermetabolism in the right vocal cord (arrow) with no activity in the left vocal cord (arrowhead). **(b, c)** Axial **(b)** and coronal **(c)** fused FDG PET–CT images of the chest show extension of the lung mass (white arrow) into the aortopulmonary window; this extension caused paralysis of the left vocal cord due to involvement of the left recurrent laryngeal nerve, thus explaining the asymmetric metabolism of the vocal cords. Also seen are encasement and marked narrowing of the left pulmonary artery (black arrows) by the mass, thus illustrating the detail seen with PET-CT. Arrowheads in **c** = aortic arch.

focal lesion or mass, as the uptake of FDG in normal muscles is diffuse and frequently symmetric. Similarly, it is easy to distinguish physiologic uptake of FDG by normal structures such as the kidney, bowel, and liver by comparison with the CT images. Occasionally, asymmetric muscle activity may occur due to paralysis of a group of muscles (Fig 30).

Advantages of PET-CT

PET-CT imaging offers some major advantages over PET imaging:

1. To our knowledge, there are no studies comparing PET or CT with PET-CT for accuracy of localization of small areas of radiotracer uptake; however, in our experience, PET-CT has been helpful in accurate localization of small areas of increased radiotracer activity that would have been difficult or not possible to localize on PET images alone (Fig 31). It also helps in distinguishing structures that normally show high metabolic activity (Fig 32) from those with abnormally increased activity (Fig 33).

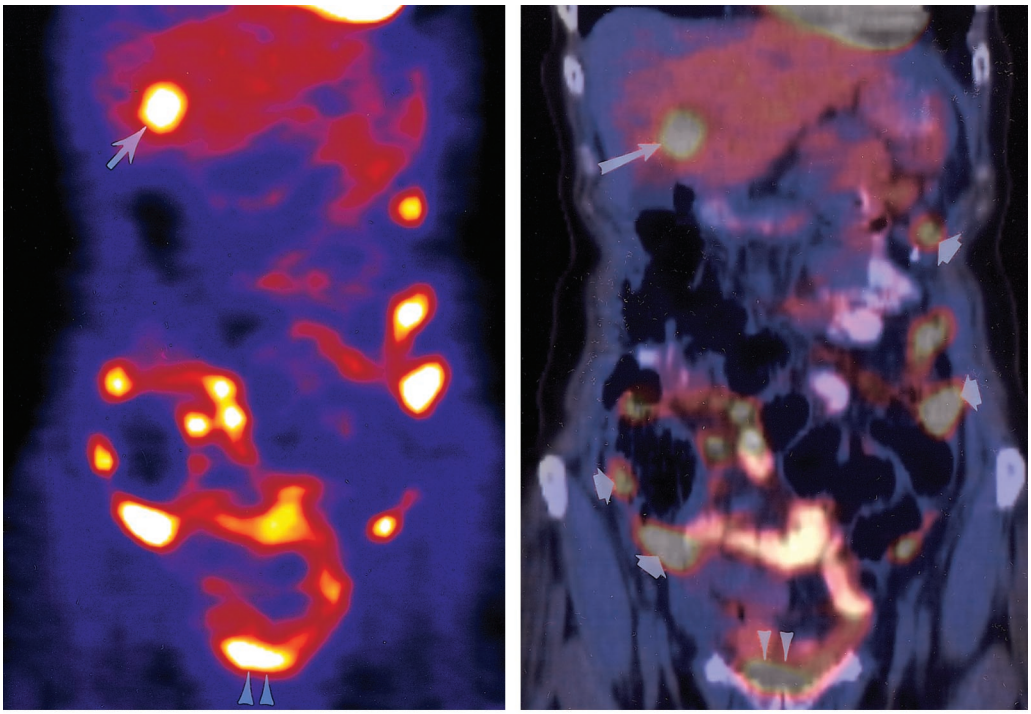

a. b.

Figure 31. Metastatic disease in a 69-year-old woman with a rising level of CA-125 antigen after resection and chemotherapy of an ovarian carcinoma. FDG PET–CT was performed to evaluate for recurrence. Arrowheads = urinary bladder. **(a)** Coronal FDG PET image shows focal hypermetabolism in the liver (arrow), a finding suggestive of metastatic disease. Scattered foci of hypermetabolism in the abdomen and pelvis have the distribution of bowel loops. **(b)** Corresponding fused FDG PET–CT image shows hepatic metastatic disease (long arrow). The abdominal and pelvic hypermetabolic foci are due to diffuse peritoneal metastases (short arrows).

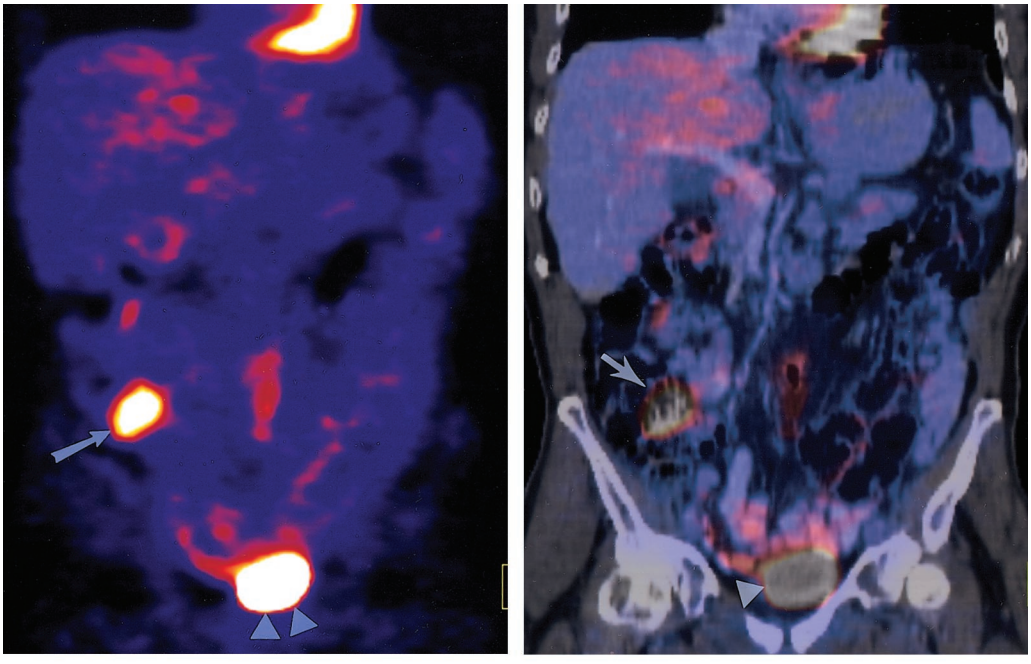

a. b.

Figure 32. Diffuse large B-cell lymphoma evaluated with FDG PET–CT before therapy. Arrowheads = urinary bladder. **(a)** Coronal FDG PET image shows focal intense hypermetabolism in the right side of the pelvis (arrow). **(b)** Corresponding fused FDG PET–CT image shows that the focus of hypermetabolism is in the cecum (arrow), a common site of physiologic activity. PET-CT helps in accurate localization of normal and abnormal FDG activity.

Figure 33. Non-Hodgkin lymphoma in a 67-year-old woman. Pretherapy FDG PET–CT was performed for staging. **(a)** Axial FDG PET image of the abdomen shows multiple areas of intense hypermetabolism that are difficult to localize except for a hypermetabolic focus in the posterior midline (arrow), which is in a lumbar vertebra. However, it is difficult to accurately localize the site of uptake within the vertebra—information that may be useful for biopsy guidance. **(b)** Corresponding fused FDG PET–CT image shows that the hypermetabolic foci are localized to a right perirenal mass (large arrowhead); pericaval and left retroperitoneal lymph nodes (short arrows); the left pedicle, adjacent body, and pars interarticularis of L4 (long arrow); and physiologic uptake in the lower pole of the left kidney (small arrowheads). Despite chemotherapy, the lesions were larger at subsequent imaging.

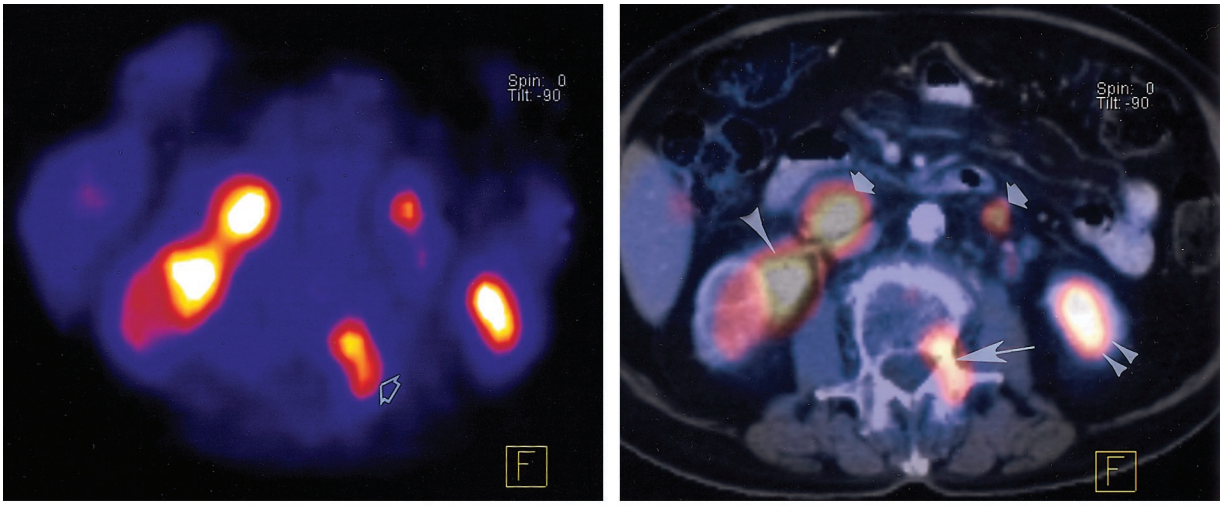

a. **b.**

2. PET-CT combines the advantages of the excellent functional information provided by PET and the superb spatial and contrast resolution of CT (Fig 30). The CT portion of the examination may demonstrate other diseases important in the clinical care of patients (Fig 34).

3. Finally, attenuation correction for quantitative or semiquantitative assessment of data is possible by using the CT data, as described earlier.

Conclusions

Detection of coincidence photons emitted during positron annihilation is the key to PET imaging, whereas accurate coregistration of this quantitative/functional information with the CT data is the key to successful PET-CT imaging. Specific attention to patient preparation, data acquisition, data reconstruction, and image interpretation is crucial to obtaining high-quality PET-CT images. Fusion of the anatomic and functional images by using a dedicated PET-CT scanner is exploited for optimal results required in the management of complex clinical scenarios faced by our clinical colleagues.

Acknowledgments: We thank David Townsend, PhD, and Scott Mason, PhD, for their help in the preparation of the manuscript and Eric Jablonowski for his help with the illustrations.

References

1. Gupta NC, Frank AR, Dewan NA, et al. Solitary pulmonary nodules: detection of malignancy with PET with 2-[F-18]-fluoro-2-deoxy-D-glucose. Radiology 1992; 184:441–444.
2. Vesselle H, Schmidt RA, Pugsley JM, et al. Lung cancer proliferation correlates with [F-18]fluorodeoxyglucose uptake by positron emission tomography. Clin Cancer Res 2000; 6:3837–3844.
3. Hoh CK, Glaspy J, Rosen P, et al. Whole-body FDG-PET imaging for staging of Hodgkin's disease and lymphoma. J Nucl Med 1997; 38:343–348.
4. Tse N, Hoh C, Hawkins R, et al. The application of positron emission tomography imaging with fluorodeoxyglucose to the evaluation of breast disease. Ann Surg 1992; 216:27–34.
5. Adler LP, Crowe JP, al-Kaisi NK, Sunshine JL. Evaluation of breast masses and axillary lymph nodes with [F-18]2-deoxy-2-fluoro-D-glucose PET. Radiology 1993; 187:743–750.
6. Strauss LG, Clorius JH, Schlag P, et al. Recurrence of colorectal tumors: PET evaluation. Radiology 1989; 170:329–332.
7. Miraldi F, Vesselle H, Faulhaber PF, Adler LP, Leisure GP. Elimination of artifactual accumulation of FDG in PET imaging of colorectal cancer. Clin Nucl Med 1998; 23:3–7.
8. Eubank WB, Mankoff DA, Schmiedl UP, et al. Imaging of oncologic patients: benefits of combined CT and FDG PET in the diagnosis of malignancy. AJR Am J Roentgenol 1998; 171:1103–1110.
9. Wahl RL, Quint LE, Cieslak RD, et al. Anatometabolic tumor imaging: fusion of FDG PET with CT or MRI to localize foci of increased activity. J Nucl Med 1993; 34:1190–1197.

Figure 34. The CT portion of a PET-CT study can demonstrate diseases besides the primary malignancy that may be important in patient care. **(a)** FDG PET–CT was performed after surgical resection of the primary tumor in a patient with colorectal carcinoma to evaluate for recurrence. Axial fused FDG PET–CT image shows extensive segmental occlusive and subocclusive pulmonary emboli (arrows), findings that would be missed with PET. **(b)** FDG PET–CT was performed for staging in a patient with Hodgkin lymphoma. Axial fused FDG PET–CT image of the brain shows an aneurysm of the right middle cerebral artery (long arrow). Intense physiologic metabolism of the brain would mask this lesion on PET images. Short arrows = misregistration due to patient motion. **(c)** FDG PET–CT was performed for restaging in a 71-year-old man with melanoma who experienced new-onset hematuria. Axial fused FDG PET–CT image of the pelvis shows a polypoid bladder mass (arrow), which was the cause of the hematuria.

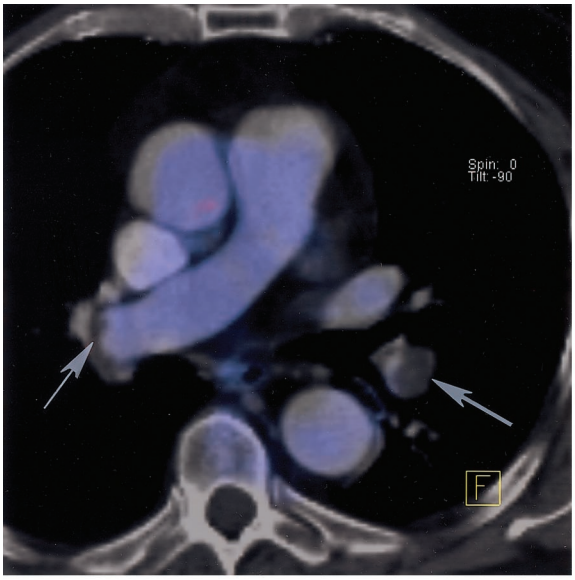

a.

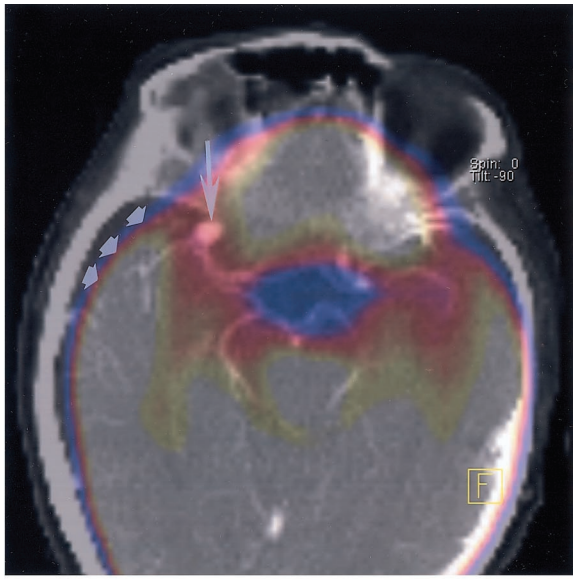

b.

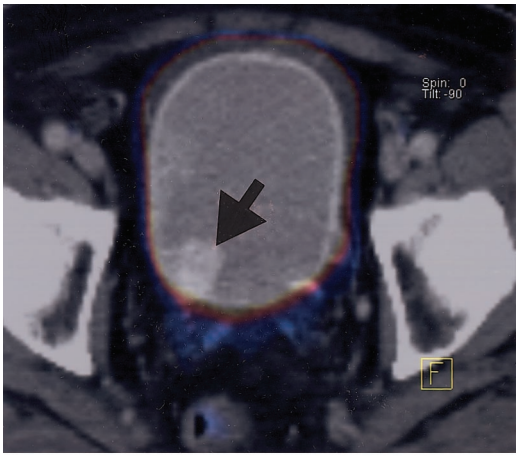

c.

10. Pietrzyk U, Herholz K, Heiss WD. Three-dimensional alignment of functional and morphological tomograms. J Comput Assist Tomogr 1990; 14: 51–59.
11. Beyer T, Townsend DW, Brun T, et al. A combined PET/CT scanner for clinical oncology. J Nucl Med 2000; 41:1369–1379.
12. Padgett HC, Schmidt DG, Luxen A, et al. Computer-controlled radiochemical synthesis: a chemistry process control unit for the automated production of radiochemicals. Int J Rad Appl Instrum [A] 1989; 40:433–445.
13. Cotran RS, Kumar V, Collins T. Neoplasia. In: Cotran RS, Kumar V, Collins T, eds. Robbins pathologic basis of disease. Philadelphia, Pa: Saunders, 1999; 260–327.
14. Smith TA. FDG uptake, tumor characteristics and response to therapy: a review. Nucl Med Commun 1998; 19:97–105.
15. Thompson CJ. Instrumentation. In: Burk ED, ed. Principles and practice of PET. Philadelphia, Pa: Lippincott, 2002; 48–63.
16. Casey ME, Nutt R. A multicrystal two dimensional BGO detector system for positron emission tomography. IEEE Trans Nucl Sci 1986; 33:460–463.
17. Beyer T, Watson CC, Meltzer CC, Townsend DW, Nutt R. The Biograph: a premium dual-modality PET/CT tomograph for clinical oncology. Electromedica 2001; 69:120–126.
18. Vesselle HJ, Miraldi FD. FDG PET of the retroperitoneum: normal anatomy, variants, pathologic conditions, and strategies to avoid diagnostic pitfalls. RadioGraphics 1998; 18:805–823.
19. Hamberg LM, Hunter GJ, Alpert NM, Choi NC, Babich JW, Fischman AJ. The dose uptake ratio as an index of glucose metabolism: useful parameter or oversimplification? J Nucl Med 1994; 35:1308–1312.
20. Kostakoglu L, Agress H, Goldsmith SJ. Clinical role of FDG PET in evaluation of cancer patients. RadioGraphics 2003; 23:315–340.
21. Let's play PET CD-ROM. Los Angeles, Calif: Crump Institute for Molecular Imaging, University of California, Los Angeles, School of Medicine, 1994–2003.